Composites for Lightweight Structures

Part A

1. Free-Body Diagram and Tip Deflection Prediction

1.1 Free-Body Diagram and Shear and Bending Moment Diagram

The cantilevered wing substructure was analysed under the limit load with a shear stress of 9.8MPa applied at the at $45°$ in the xy-plane over the tip rib. The perimeter of the root is fully restrained. The wing was modelled as a cantilever beam with a span L=130mm. The tip rib's cross section was found to be $324+9\pi$ mm^2 which yields F=3452.29N. The free-body diagram shows the wing with F as the applied force where x=0 at the root and x=L at the tip.

$$V_x = V_y = -F_{x,y} = -2441.14N \tag{1}$$

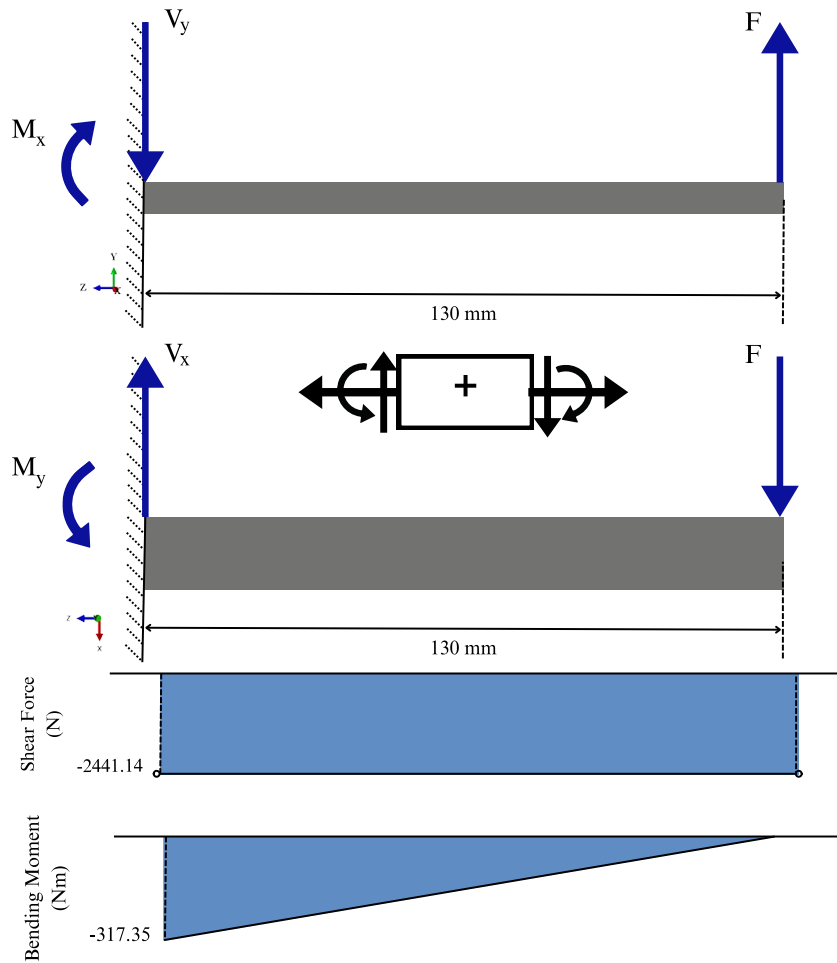$$M(x) = (F_x)(L-x) = 317348.2Nmm \tag{2}$$

Figure 1: Free-Body Diagram, Shear and Bending Moment Distribution over Span.

1.2 Analytical Prediction of Tip Deflection

To find the tip deflections using Euler-Bernoulli beam theory, the second moment of area of the cross section (I_{xx} and I_{yy}) was required. The cross section is symmetric about the x-axis and shown in the Figure 2. It was discretised into rectangular sections and curved edges with the thickness of the laminate considered. The E_{eff} was found to be 54.1GPa which was found using the given quasi-isotropic laminate by Composite Laminate Theory.
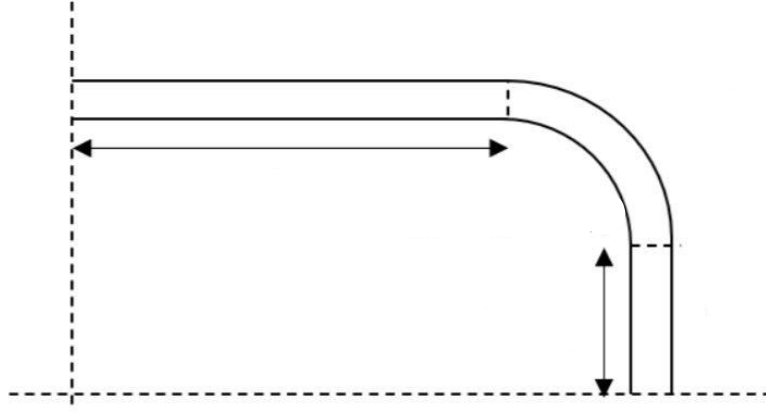
Figure 2: *Cross Section Discretised to find Second Moment of Area*

$$I_{xx} = 2393.41mm^4$$

$$I_{yy} = 20050.01mm^4$$

The tip deflections were found using the formula below.

$$\delta_x = \frac{F_x L^3}{3E_{eff}I_{yy}} = 1.65mm, \delta_y = \frac{F_y L^3}{3E_{eff}I_{xx}} = 11.25mm \tag{3}$$

These predictions assume small deformations and neglect shear effects. The larger δ_y shows that greater flexibility due to the lower I_{xx}.

---

2. Stress, Strain, and Buckling Analysis

2.1 Stress and Strain Analysis

The loads acting on the root were determined from equilibrium.

$$R_{x,y} = -2441.14N$$

$$M_0 = -317348.2Nmm$$

The plane stress assumption was used because the stress component (σ_{yy}) in the y-direction was 0. At the midplane of the top ply (σ_{xx}) also equals zero because it lies on the neutral axis. σ_{zz} was determined using the equation below where M_x is the moment about the x-axis and y is the distance from the neutral x-axis.

$$\sigma_{zz} = \frac{M_x y}{I_{xx}} = 539.8MPa \tag{4}$$

To calculate the strain, Equation 5 was used where it integrates σ_{zz} across the top cover thickness of 1.6mm with the midplane at 5mm from the neutral axis resulting in the stress resultant of N_{zz}.

$$N_{zz} = \int_{4.2}^{5.8} \sigma_{zz} dy = -863.7N/mm \tag{5}$$

$N_{xx} = 0$ because $\sigma_{xx} = 0$. The transverse shear stress τ_{zx} was integrated to find the shear stress across the top ply where A is the area of the top cover, and x is the distance to the y axis and b is the width of the top cover where the shear force is applied on resulting in the equation below.

$$N_{xz} = \int_{4.2}^{5.8} \tau_{zx} dy = \int_{4.2}^{5.8} \frac{S_x A x}{I_{yy} b} dy = 0 \tag{6}$$

This shows that there is no shear force in the middle of the top cover. The ABD matrix was used from the material properties and eLamX to find the strains which were ε_z=-0.0099 and ε_x=0.031 γ_{xz}=0

$$\begin{bmatrix} N \\ M \end{bmatrix} = \begin{bmatrix} A & B \\ B & D \end{bmatrix} \begin{bmatrix} \varepsilon \\ \kappa \end{bmatrix} \tag{7}$$

2.2 Buckling Analysis

This analysis assumes uniaxial compression loading on the top covers with $N_y = N_{xy} = 0$. The covers were modelled as orthotropic laminates which was simply supported on all the sides with $D_{16} = D_{26} = 0$. The critical buckling stress was calculated using the Equation 8 where a and b are the dimensions of the cover and m is the buckling mode number.

$$N_{crit} = \frac{\pi^2}{b^2}\left(D_{11}\frac{m^2 b^2}{a^2} + 2(D_{12} + 2D_{66}) + D_{22}\frac{a^2}{m^2 b^2}\right) \tag{8}$$

To identify the minimum N_{cr}, the two close integer values of m were tested and found to be at mode 2. This was then used to find the bending moment using the equation below.

$$N_{crit} = \int_{4.2}^{5.8} \frac{M_x y}{I_{xx}} dy = 994.8 N/mm \tag{9}$$

The moment was divided by the length of the root to determine the tip shear force and then divided by the tip area of $(324+9\pi)mm^2$ to compute the buckling load which resulted in 22.56MPa for the outboard cover and 11.29MPa for the inboard cover.

3. Finite Element Analysis in Abaqus CAE

3.1 Tip Deflection Comparison

To evaluate the wing substructure's response under the limit load where a load of 9.8MPa was applied as a shear stress at 45 degrees on the tip rib, finite element analysis was conducted using Abaqus. Two analyses were conducted: a linear and a nonlinear static analysis. For the linear static analysis, the Static, General step was employed with the nonlinear geometry option (NLGEOM) disabled, assuming small deformations and a linear elastic response. For the nonlinear analysis, the same step was used but NLGEOM was enabled to account for geometric linearity due to potentially large deformations or buckling effects. The type of load applied used the surface traction option in Abaqus. Tip deflections in the horizontal and vertical directions were extracted from the tip rib's loaded edge for both analyses. The results are summarised in Table 1 below.

Table 1: Tip deflections from analytical, linear and nonlinear analyses.

Analysis	δ_x (Horizontal)	δ_y (Vertical)
Linear	1.84 mm	12.28mm
Nonlinear	1.91mm	13.39mm
Analytical	1.65mm	11.25mm

The nonlinear analysis produced higher deflections compared to the linear analysis due to the geometric nonlinearity which plays a significant role under the applied force because it considers large deformations, rotations and changes in the structure's stiffness. The linear analysis assumes small strains and underestimates the deformation by maintaining a constant stiffness matrix while the nonlinear analysis accounts for load reorientation and transverse shear, which amplifies δ_y due to the bending dominance. The analytical prediction based on Euler-Bernoulli beam theory with $E_{eff} = 54.1GPa$ and isotropic material properties and neglects rib stiffness variations and shear deformations thus underestimating deflections. The δ_x smaller increase suggests that the 0° plies at the root resist horizontal deformation more effectively. In addition, the increased deflections from the nonlinear analysis may be attributed to the wing's susceptibility

to buckling which will be discussed in the following sections. The nonlinear analysis is more representative of the wingbox behaviour under the limit load because this structure permits post buckling deformations, however linear analysis is useful for initial sizing due to its computational efficiency. The analytical predictions from Section 1.2 align more closely with the linear FEA results likely because the hand calculations assumed small deflections and neglected nonlinear effects such as post-buckling deformation.

3.2 Linear Prediction of First Instability

A linear buckling analysis was performed by employing the linear perturbation, buckle step. The applied load was normalised to 1MPa to enable Abaqus to output the eigenvalues as the critical load. The analysis assumes linear elastic behaviour and does not account for material nonlinearity and geometric imperfections. The first eigenvalue had a value of -10.709 and this suggests a reverse buckling mode under a load reversal which is opposite to the applied direction.

The first buckling mode occurred at a critical load of 10.709MPa, based on the undeformed geometry and the boundary conditions specified at the root. The mode shown in Figure 3 shows that there is local buckling of the upper wing skin near at the root which was driven by compressive stresses induced by the shear load and cantilever bending. The buckling shape shows a single sinewave along the span.
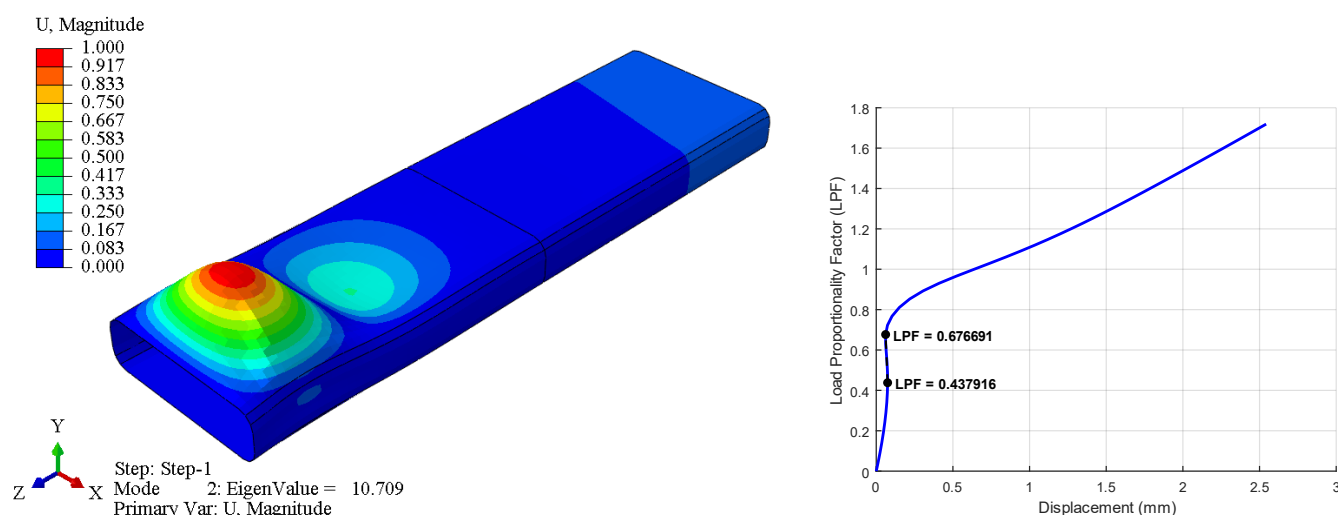

Figure 3: (a) Contour plot of the first buckling mode shape from linear analysis. (b) Graph of load factor (LPF) versus displacement magnitude for the nonlinear buckling analysis.

This shows that the wing buckles just beyond the limit load and comparing it to hand calculations, the FEA result is higher. This discrepancy arises from the simplified assumptions like simply supported edges and uniform compression. The analytical calculations simplified the geometry to a 2D plate, neglecting the 3D interactions with the ribs and spars.

The FEA's higher prediction reflects its ability to model the whole structure including the rib-spar interactions. The FEA result of 10.709 MPa appears more accurate than the hand calculations which are 11.29MPa, as it accounts for the complex stress state and structural details omitted in analytical models. However, its linear nature assumes perfect geometry and elasticity, potentially overestimating stability compared to nonlinear effects as shown in the next section. The linear analysis also shows that buckling does not initiate under the limit load. It overpredicts the stability compared to the nonlinear analysis highlighting the need for a combination of approached to assess buckling accurately.

Method	Critical buckling load
Linear (FEA)	10.709 MPa
Analytical (Hand)	11.29 MPa
Nonlinear (FEA)	4.29 MPa

3.3 Nonlinear Onset of First Instability

A geometric nonlinear analysis was performed using the Riks method with the NLGEOM option enabled to predict the buckling onset under the limit load. The Riks method was chosen to capture the buckling and post-buckling behaviour by tracking the load proportionality factor (LPF) and the magnitude of the displacement (U). To initiate the analysis an imperfection of 0.001mm was introduced based on the linear buckling mode shape from Section 3.2. This was introduced to make the structure more susceptible to local instability as without it the structure is perfect and may lead to exhibit unrealistically high buckling resistance. The displacement was monitored at the node which had the maximum deformation in the linear buckling analysis to ensure that we track the buckling response accurately.

The LPF vs U plot is shown in Figure 3(b) and shows that it exhibits a nonlinear response. The curve rises linearly to around an LPF of 0.4 with a maximum displacement of less than 0.1mm and then exhibits a slope change at LPF = 0.438, indicating buckling at 4.29MPa. Post buckling the structure can carry more load with LPF increasing linearly from 0.8 to 1.6. The two points marked in Figure 3 are where buckling starts and then stabilises. The structure snaps from that point to the next. Compared to the linear and analytical prediction the nonlinear critical load at 4.29MPa is 60% lower. The linear analysis overestimates stability by assuming perfect geometry and elasticity while the analytical assumes a simply supported plate under uniaxial compression. The Riks method, the most accurate prediction, which includes geometric nonlinearity and imperfections trigger early buckling showing that the structure is susceptible to compressive stresses. In addition, it is more accurate cause it is validated by the post buckling agreement with the design requirements, so it is the more reliable estimate.

4. Design Criteria Evaluation

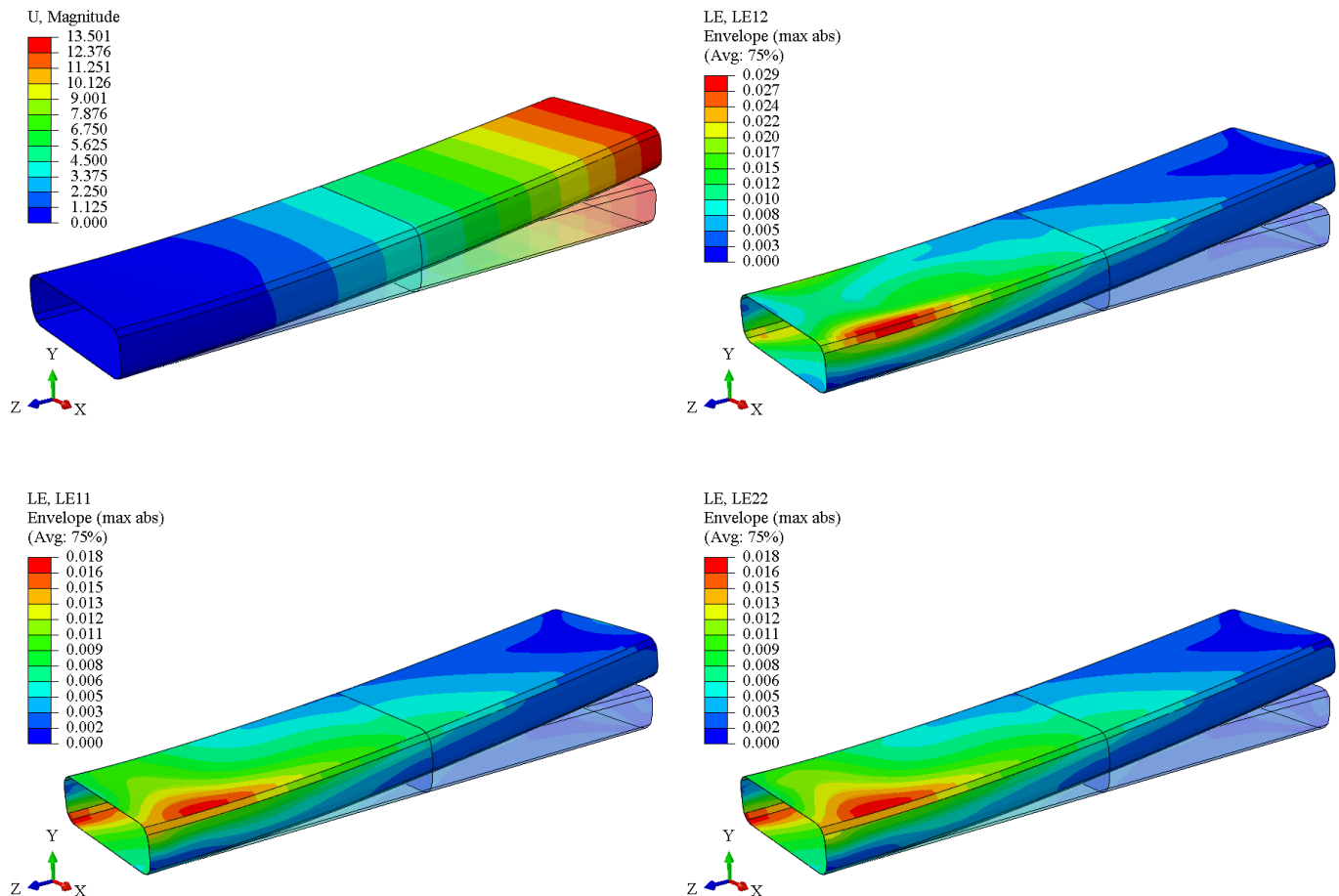### 4.1 Contour Plots of Displacements and Strains

Contour plots of displacements and strains were generated from the nonlinear analysis conducted in the section above. Figure 4(a) shows the tip deflections and reveal a gradient of deformation with a max displacement at the tip and near zero near the root. The strain contour plots highlight the longitudinal strain (LE11), transverse strain (LE22) and the shear strain (LE12) where it peaks at 0.018, 0.018 and 0.029 respectively. LE11 and LE22 peaks at the root cover and the bottom of the curved root spar on the far side. LE12 peaks at the top of the root spar on the near side. The 0° plies in the root layup resist longitudinal deformation, constraining U1, while the 45° load amplifies U2 through shear-bending coupling. The LE12 peak (0.029) at the root spar's top (near side) aligns with the ±45° plies' shear resistance under the 45° load. The results' accuracy relies on mesh refinement, which appears sufficient given smooth gradients, though finer elements could refine strain peaks.

4.2 Failure Load and Tip Deflection at Limit Load

Table 2: Hashin's Failure Criteria

Ply	Angle	HSNFCCRT F= 7.081MPa	HSNFTCRT F= 9.781 MPa	HSNMCCRT F= 8.749 MPa	HSNMTCRT F= 7.081 MPa
1	-45°	0.2380	0.2620	0.3890	1.0400
2	+45°	0.4920	0.3220	0.3380	0.9560
3	90°	0.0981	0.1480	0.0458	1.0500
4	0°	1.0600	1.0100	0.1090	0.0904
5	-45°	0.2150	0.2360	0.2530	1.0500
6	+45°	0.4420	0.3340	0.3270	0.9230
7	90°	0.0977	0.0499	0.0396	1.0300
8	0°	1.0400	0.9990	0.0649	0.0945
9	0°	1.0300	0.9970	0.0618	0.0956
10	90°	0.0974	0.8080	0.0530	1.0200
11	-45°	0.3830	0.3500	0.4680	0.0883
12	+45°	0.1770	0.1940	0.6360	1.0500
13	0°	1.0000	0.9890	0.0419	0.1010
14	90°	0.1030	0.2660	0.0458	1.0100
15	-45°	0.3410	0.3630	0.8730	0.0872
16	+45°	0.1830	0.1720	1.0900	1.0500
δ_x (Horizontal)		1.348 mm	1.904 mm	1.683 mm	1.348 mm
δ_y (Vertical)		9.112 mm	13.4 mm	11.56 mm	9.112 mm

The structure first fails at 7.08MPa due to fibre compression. The primary failure mode is fibre compression in 0° plies and matrix tension at -45° and 90° in the upper level of the midplane and +45° and 90° at the lower level of the midplane. The matrix tension failure occurs at the bottom left spar near the root and the fibre compression at the top right root cover. Table 2 summarises the Hashin indices for all the plies at their critical load showing where the first plies fail and their respective deflections. At 9.8MPa indices increase further indicating progressive damage.

The wingbox undergoes bending because the 0°plies are responsible for carrying the axial loads and because of the applied shear load causing compressive stresses on the upper skin and tensile stresses at the bottom skin. For fibre tension, the 0° plies failed for the same reason.

The matrix compression failure in the +45 ply of the bottom skin is due to the combined shear and transverse compression. The ±45° plies carry shear loads, which generate transverse tensile stresses in the matrix. As the shear load increases, the matrix tensile strength is exceeded, resulting in micro-cracking and eventual failure. Figure 5 shows the most critical regions of failure according to Hashin's criteria.
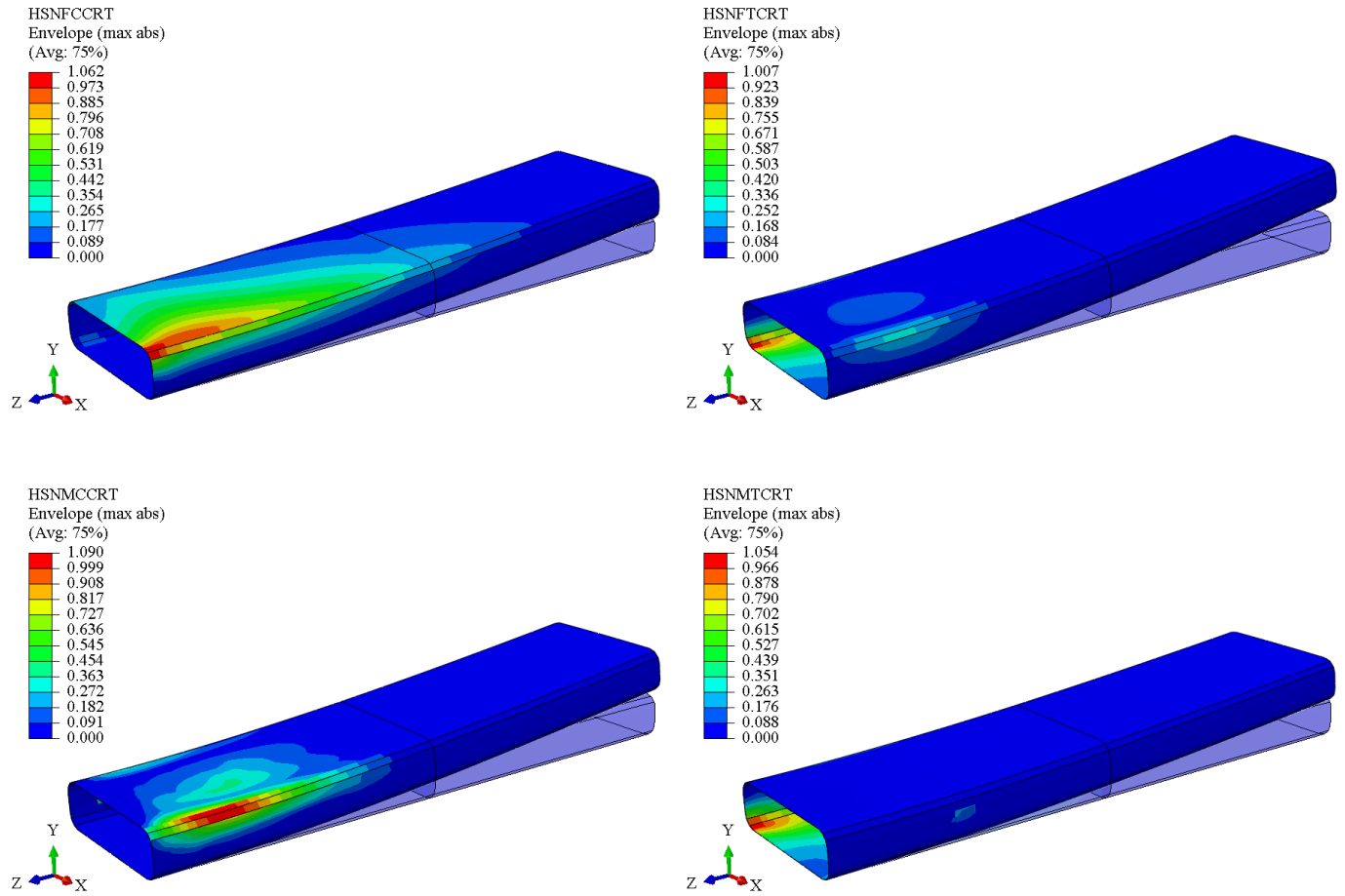
Figure 5: Contour plots for Hashin Criteria at different critical loads.

The contour plots show that failure initiates in two primary regions which are consistent with the high strains observed in Section 4.1. Fibre compressive failure near the root aligns where the longitudinal and transverse strain is peak, as this is due to the bending stresses. Matrix tension failure occurs at the top of the root spar and corresponds to the shear strain showing that matrix cracking has initiated due to shear and transverse tension in those failed plies.

4.3 Compliance with Design Constraints

Table 3 outlines the design constraints and assesses the compliance of the current design. This design requires optimisation to reduce the vertical tip deflection and increase the failure load to 9.8MPa while maintain compliance with the other criteria.

Table 3: Evaluation of Design Constraints

Criteria	Required Values	Actual Value	Satisfied
Vertical Tip Deflection	≤ 12 mm	13.372 mm	No
Horizontal Tip Deflection	≤ 2 mm	1.904 mm	Yes
Material Damage	Not Allowed	Failure at 7.08MPa (Hashin)	No
Buckling Stability	Tolerated	Buckling at 4.29MPa, stable to 9.8MPa	Yes
Maximum Mass	≤ 31.75 g	30.63 g	Yes
Laminate Constraints	Balanced and Symmetric		Yes

5. Design Optimization

To mitigate the design deficiencies identified above the substructure was optimized by modifying the laminate layup configuration. Due to the symmetry, only half of the new sequence is provided in Table 5, while the full stacking sequence is shown in Figure 6.

Table 5: *Optimised Layup for Covers and Spars.*

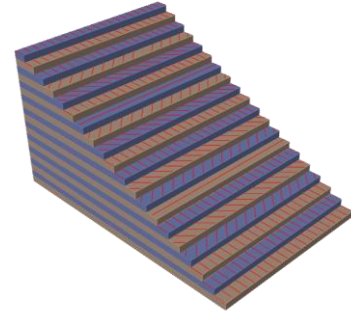| Ply	Ribs	Root Covers and Spars	Tip Covers and Spars
1		0	
2		0	
3		0	
4		-45	-45
5		45	45
6		0	0
7	-45	90	90
8	45	-45	-45
9	90	45	45
10	0	0	0

Figure 6: *Layup in the Root Cover*

The upper and lower root covers and spars use a [(0,0,0,-45,45,0,90,-45,45,0)]$_S$ layup, a symmetric 20-ply laminate with additional 0-degree plies to boost bending stiffness. The upper and lower tip covers and spars adopt a thinner [(-45,45,0,90,-45,45,0)]$_S$ layup, a symmetric 14-ply laminate, to reduce weight while maintaining adequate strength for the lower loads at the tip. The ribs retain a [(-45,45,0,90)]$_S$ layup, an 8-ply quasi-isotropic laminate, ensuring balanced properties for shear resistance. All layups are balanced and symmetric, meeting laminate constraints. Figure 7 show the Hashin's criteria at the limit load and Table 6 shows that all the constraints have been met.

Table 6: *Comparison of Original and Optimised Design Performance*

| Criteria	Required	Original	Optimised	Satisfied
Vertical Tip Deflection	≤ 12 mm	13.372 mm	8.096 mm	Yes
Horizontal Tip Deflection	≤ 2 mm	1.904 mm	1.233 mm	Yes
Material Damage	Not Allowed	Failure at 7.08MPa	Failure at 12.49MPa	Yes
Buckling Stability	Tolerated	Buckling at 4.29MPa	Buckling at 7.35MPa	Yes
Maximum Mass	≤ 31.75 g	30.6292 g	31.5327 g	Yes
Laminate Constraints	Balanced and Symmetric			Yes
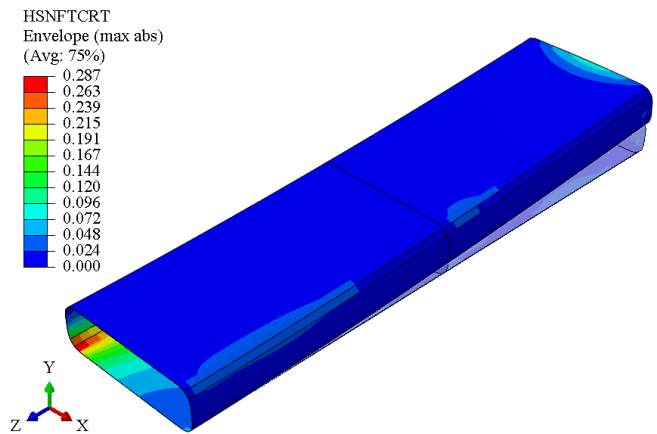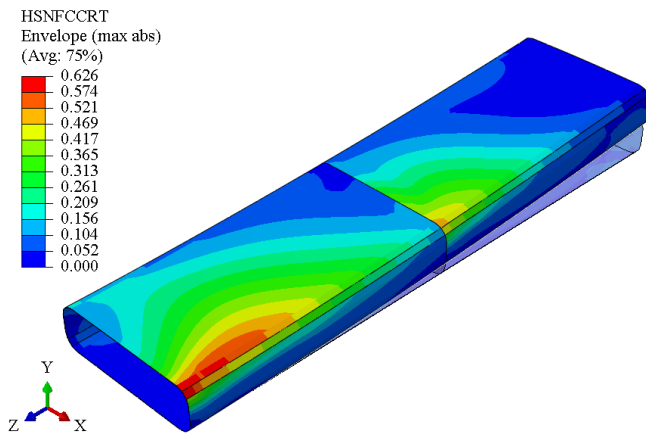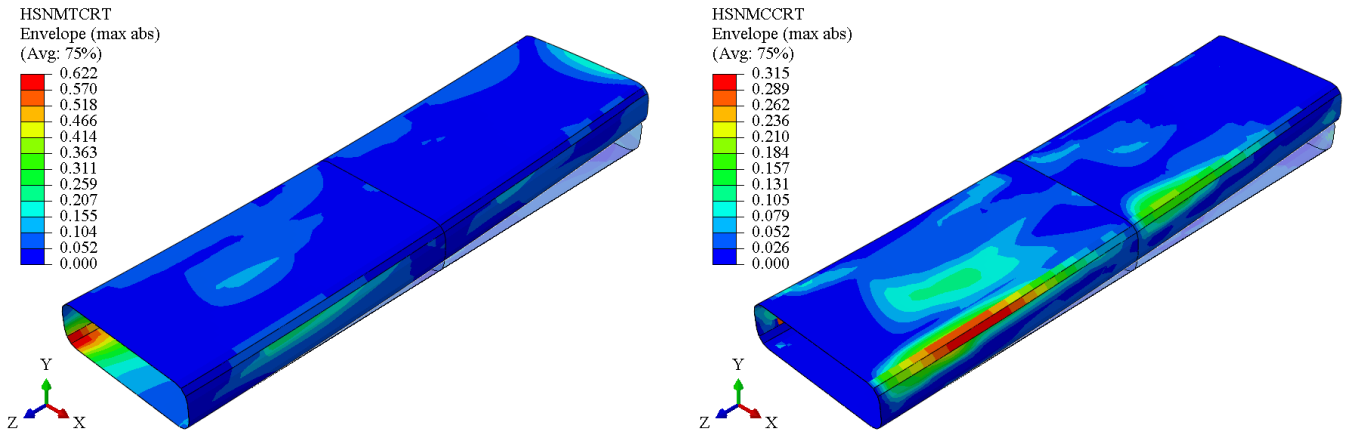
Figure 7: Contour plots illustrating Hashin's failure criteria for a limit load of 9.8MPa for the optimised layup.

6. Performance Comparison of Optimized Design

The design philosophy was to meet the vertical tip deflection limit so more 0° plies were added which provided more resistance to axial loading. Strengthening the root was vital as this had most of the bending moments and stresses acting on it then plies were subtracted from the rib and the tip because it had to meet the mass requirement. In the root 0° plies were prioritised to prevent fibre compression failure especially under large bending loads. At the tip used more ±45° fibres to align with the applied 45° load direction, improving shear and bending resistance. There was an attempt to use fewer plies to make the structure as lightweight as possible however the mass requirement was critical. A more pronounced philosophy would be to counter the compressive stresses at the lower region and the tensile stresses at the upper cover. For every ply that failed in the load direction means that we have to add more of those plies to carry the same load and conversely for the matrix there will be more of the opposite direction/ perpendicular. This is due to laminates were best at the fibre direction also the further away the plies are from the neutral axis the more effective they are.

The optimised layup sacrifices quasi-isotropic stiffness to prioritise the 45° tip shear load. While this reduces multi-directional load capability, it eliminates shear extension coupling by being a balanced laminate. The inboard region is dominated by 0° plies to resist bending moments as they are the highest at the root and consequently increasing D_{11}. This also limits the tip deflections and delays buckling in the inboard region as that is where compressive stresses peak. The outboard region is thinner with ±45° plies to reduce mass and to maintain the shear and buckling resistance as it increases the D_{66} term as it enhances shear stiffness. The ribs have a symmetric and balanced layup to ensure shear stability with minimal weight. The 90° plies stabilise transverse deformations which was deemed not necessary as D_{22} played a minimal role in the ABD matrix. Since shear dominated in the outboard region, ±45° plies enhance D_{12} and D_{66} which is critical for shear buckling. In low stress regions, ply drops were done to reduce weight. Since the design requirements state that buckling is tolerated, it was not a priority to optimise a layup based on it, thus having low amount of ±45° plies at the outboard. Moreover, having more ±45° plies will increase impact resistance.

The optimised layup fails at 12.49MPa and the failure mode is fibre compression and matrix tension according to the Hashin's criteria. The -45° plies fail first so it could have been moved towards the outward of the midplane to increase D_{66}. After conducting the damage progression analysis, the buckling load was found to be where the largest amount of energy was dissipated, and it was found to be 12.53MPa.

Another method of optimising the layup was to use lamination parameters to enhance buckling or stiffness of the structure. The limitations of this method were that there would be multiple layups that can meet the required lamination parameters.

7. Progressive Damage Analysis for Ultimate Load

A progressive damage analysis was conducted on the optimised design, progressively increasing the load from the limit load to the ultimate load of 14.7MPa. The optimised design does not reach the ultimate load and structurally collapses at 13.36 MPa which is at an LPF of 0.91. The structure can only sustain an additional 0.347MPa after damage initiates in the tension of the fibre. Fibre compression failure initiates at the inboard upper cover and spar, where the bending stresses are the highest at 12.53MPa. Then matrix compression occurs at the inboard root spar following fibre compression failure at 12.58MPa due to the deformation and failure of the fibre compression. Matrix tension initiates at the lower edge of the tip rib because of the shear force applied at 12.99MPa. Then damage initiates for the fibre tension at 13.01MPa at the edge of the tip rib. Then the structure collapse at 13.36MPa. This shows that post fibre tension failure, the substructure exhibited rapid energy released indicating that the remaining plies do not have enough residual strength. Figure 8 shows the damage of the structure, and the graph of energy dissipated where spikes indicate failure events. Fibre dominated failure releases very high energy while matrix dominated failure dissipates energy gradually. Since most of the damage occurred at the tip rib, ±45° plies should be added to the tip ribs for enforcement.
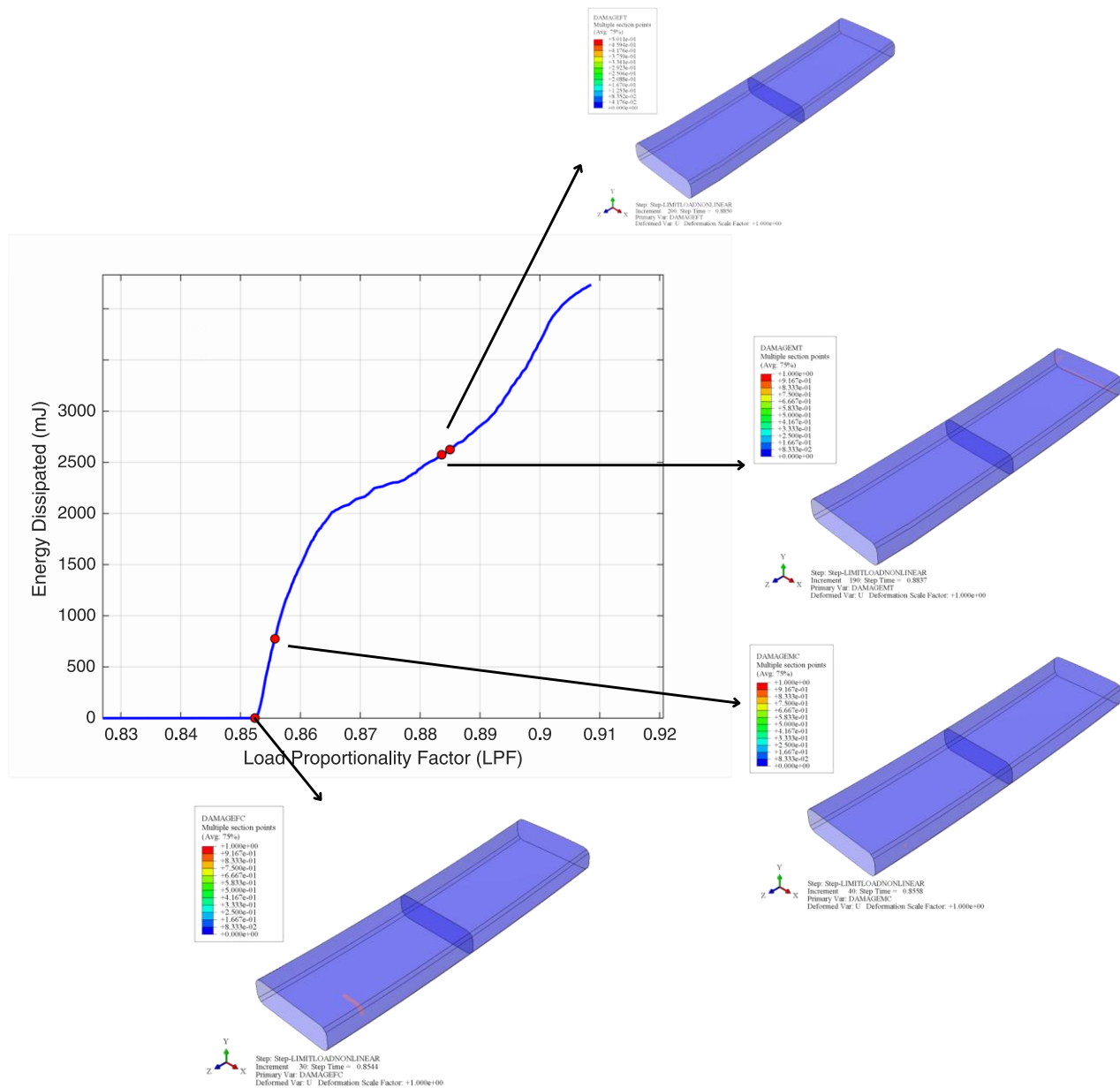

Figure 8: Damage initiation using Energy Dissipated Graph

Part B

The key differences between my design and my peer's design is having different priorities in optimisation. In the inboard section, I prioritised the 0° plies at the outer layers to maximise bending stiffness while my peer used ±45° exterior plies for buckling and impact resistance. This resulted in having lower tip deflections in both directions compared to my peer's design. This was effective for meeting the deflection limits but had less buckling resistance cause the new layup did not contribute to terms D_{12} and D_{66}. Alternatively, my peer used ±45° plies on the exterior in the inboard section to enhance buckling and impact resistance at the expense of a higher mass. In the outboard section, I included four extra plies to ensure that shear loading would be carried while my peer minimised mass in this low stress region. However, both of us have acknowledged that ribs are non-critical as we minimised the ply count but in different orders. Also, we both met all the design requirements stated in the brief.

Another difference is our optimisation philosophy, where my rationale was suitable for applications where deflections are critical and loads are predictable, however my peer's rationale aligns with aerospace certifications where fail safe design is critical. The key insight was that my peer improved the D_{66} term to increase buckling resistance to which I did not consider as I favoured bending performance. Moreover, I could have also done more on the buckling resistance as my initial design was based on the requirements and when the vertical tip deflection passed the maximum limit, I took it as a priority to minimize it followed by material damage at limit load.

Reflecting on my peer's design, I would redesign the inboard layup by retaining 0° plies but adding more ±45° plies on the exterior which should be more resistant to buckling. Also, I could avoid grouping identical plies to mitigate crack propagations as shown by my peer. Table 7 summarises the differences between our designs.

Table 7: Comparison between designs

Location	My Design	Peer's Design
Inboard Covers/Spars	[(0,0,0,-45,45,0,90,-45,45,0)]s	[-45,45,0,90,0,-45,45,90,0,90,0] s
Outboard Covers/Spars	[(-45,45,0,90,-45,45,0)]s	[-45,45,90,0,90,0] s
Ribs	[(-45,45,0,90)]s	[-45,45,90,0] s
Deflections	X (1.2mm) Y (8.1mm)	X (1.4mm) Y (9.1mm)
Mass	31.53g	31.6 g
Philosophy	Maximise stiffness to mass ratio	Ensure buckling resistance